Evaporation-induced cavitation in nanofluidic channels

Citation: Duan, C. et al. "Evaporation-induced Cavitation in Nanofluidic Channels." Proceedings of the National Academy of Sciences 109.10 (2012): 3688–3693. ©2012 by the National Academy of Sciences

As Published: http://dx.doi.org/10.1073/pnas.1014075109

Publisher: National Academy of Sciences

Persistent URL: http://hdl.handle.net/1721.1/74589

Version: Final published version: final published article, as it appeared in a journal, conference proceedings, or other formally published context

Evaporation-induced cavitation in nanofluidic channels

Chuanhua Duan[a,1], Rohit Karnik[b], Ming-Chang Lu[a,2], and Arun Majumdar[a,c,d,3,4]

[a]Department of Mechanical Engineering, University of California, Berkeley, CA 94720; [b]Department of Mechanical Engineering, Massachusetts Institute of Technology, Cambridge, MA 02139; [c]Department of Materials Science and Engineering, University of California, Berkeley, CA 94720; and [d]Materials Sciences Division, Lawrence Berkeley National Laboratory, Berkeley, CA 94720

Edited by Andrea Prosperetti, Johns Hopkins University, Baltimore, MD, and accepted by the Editorial Board January 10, 2012 (received for review September 19, 2010)

Cavitation, known as the formation of vapor bubbles when liquids are under tension, is of great interest both in condensed matter science as well as in diverse applications such as botany, hydraulic engineering, and medicine. Although widely studied in bulk and microscale-confined liquids, cavitation in the nanoscale is generally believed to be energetically unfavorable and has never been experimentally demonstrated. Here we report evaporation-induced cavitation in water-filled hydrophilic nanochannels under enormous negative pressures up to −7 MPa. As opposed to receding menisci observed in microchannel evaporation, the menisci in nanochannels are pinned at the entrance while vapor bubbles form and expand inside. Evaporation in the channels is found to be aided by advective liquid transport, which leads to an evaporation rate that is an order of magnitude higher than that governed by Fickian vapor diffusion in macro- and microscale evaporation. The vapor bubbles also exhibit unusual motion as well as translational stability and symmetry, which occur because of a balance between two competing mass fluxes driven by thermocapillarity and evaporation. Our studies expand our understanding of cavitation and provide new insights for phase-change phenomena at the nanoscale.

nanobubbles | confined fluids | confined water | bubble dynamics | bubble formation

Liquids are known to sustain considerable negative pressures (1–4). However, beyond a certain limit small vapor bubbles are formed, a phenomenon widely known as cavitation. Although the real "breaking" limit (the spinodal point) for homogeneous nucleation in liquids such as water is around hundreds of megapascal of negative pressure (2), heterogeneous nucleation can lead to cavitation at much lower negative pressures. Such heterogeneous nucleation has attracted significant attention in many diverse fields of science and engineering such as the design of ship propellers and various hydraulic machinery, where the impingement of vapor bubbles due to high-speed motion leads to serious erosion damage (2). Cavitation also arises in microscale-confined liquids in plants. Its occurrence in plant xylem (water transport microchannels) (1–4) and the annulus cells of sporangia of ferns (5, 6) plays a role in the ascent of sap and ejection of spores, respectively. In condensed matter science, cavitation provides opportunities to study phase transitions under the influence of intermolecular forces of cohesion and adhesion at various interfaces. Despite these studies in bulk and microscale, cavitation in nanoscale confined liquids, which offers extremes of negative pressures and intermolecular forces, has not been observed or studied. It has been pointed out that cavitation is energetically unfavorable in nanochannels with uniform contact angle and channel size, because the critical size of nucleating vapor bubbles is comparable to the smallest dimension of the nanochannel (7, 8). Here we show that gas-seeded vapor bubbles can occur and grow unlimitedly during evaporation of liquids confined inside the channel. The dynamics of such cavitation in 20–120 nm nanochannels are studied and quantitatively compared with a series of analytical models based on evaporation.

Cavitation experiments were performed in silica nanochannel devices fabricated using sacrificial layer etching and microchannel bonding (see *SI Appendix*) (9). As shown in Fig. 1 and *SI Appendix*, Fig. S1, there are in all two microchannels separated by a gap and nine sets of staggered nanochannels in each device. Each set of nanochannels includes 10 individual nanochannels, which are 120-μm long and 4-μm wide. These nanochannels are located on the same horizontal plane, which is 2-μm below the bottom surface of the microchannels. Each set of nanochannels communicates with the microchannels through access holes that are perpendicular to the microchannel bottom surface at two ends of the channels. Out of these nine sets, there is only one set of channels bridging the two microchannels (referred as bridging nanochannels), which acted as reference channels for measurement of channel height via ionic conductance (9). The other sets of nanochannels, referred as nonbridging nanochannels, are embedded inside the microchannels with access holes on either ends of the nanochannels connecting to the same microchannel (Fig. 1*C*). These nonbridging nanochannels with two ends in the same microchannels were used to monitor the cavitation experiments. The original channel height (20–30 nm) was defined by the thickness of the sacrificial polysilicon layer, which could be increased up to 120 nm in a controlled manner by gradual etching in 30% wt/wt KOH at room temperature (see *SI Appendix*). Such etching did not result in tapered structures, as demonstrated elsewhere (10). SEM images of channel cross-section and studies of diffusion limited reaction (10) also confirmed a uniform channel height along the length of the nanochannels, except close to the entrance (see *SI Appendix*). Surface contact angle measurements showed that the channel surfaces remained hydrophilic, and atomic force microscopy studies revealed a surface roughness of less than 1 nm (see *SI Appendix*).

In a typical experiment, evaporation of water occurring in a set of nonbridging nanochannels (with both ends in the same microchannel) was recorded. Deionized water was first introduced into the reservoirs of a nanochannel device treated with oxygen plasma that allowed for immediate wicking of the water into the microchannel and nanochannels. Subsequently, water in the reservoirs was removed and the device was left in the atmosphere for evaporation to occur (*SI Appendix*, Fig. S10*A*). It was

Author contributions: C.D., R.K., and A.M. designed research; C.D., R.K., M.-C.L., and A.M. performed research; C.D. contributed new analytic tools; C.D. analyzed data; and C.D., R.K., and A.M. wrote the paper.

The authors declare no conflict of interest.

This article is a PNAS Direct Submission. A.P. is a guest editor invited by the Editorial Board.

[1]Present address: Department of Mechanical Engineering, Boston University, 110 Cummington Street, Boston, MA 02215.

[2]Present address: Department of Mechanical Engineering, National Chiao Tung University, 1001 University Road, Hsinchu 30010, Taiwan.

[3]To whom correspondence should be addressed. E-mail: Arun.Majumdar@hq.doe.gov.

[4]Present address: Advanced Research Projects Agency–Energy, US Department of Energy, 1000 Independence Avenue, Washington, DC 20585.

This article contains supporting information online at www.pnas.org/lookup/suppl/doi:10.1073/pnas.1014075109/-/DCSupplemental.

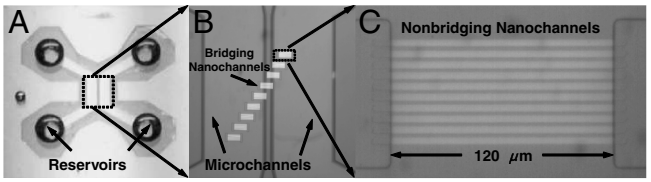

Fig. 1. Transparent nanochannel device. (*A*) A bonded nanochannel device with reservoirs on top. Each device includes two microchannels and four reservoirs. Microchannels are 1-cm long, 500-μm wide, and 40-μm deep. Reservoirs are through-holes with 1-mm diameter. (*B*) Zoom-in image of the nine sets of staggered nanochannels. Only one set of nanochannels is bridging to the two microchannels. These bridging nanochannels were used to measure channel height, whereas nonbridging nanochannels were used for cavitation experiments. (*C*) Zoom-in image of a set of nonbridging nanochannels with two ends in the same microchannel. Each set consists of 10 120-μm-long, 4-μm-wide silica nanochannels.

observed that two menisci formed at the end of the microchannel first and then one of them started receding while the other was pinned at the entrance (*SI Appendix*, Fig. S10*B*). As one of the menisci receded, a thin film of water remained in the microchannel. Once the meniscus receded completely out of the microchannel, the thin film of water remaining on the microchannel wall gradually disappeared (*SI Appendix*, Fig. S10*C*). Water in the nonbridging nanochannels started evaporating only after water in the corresponding microchannel had completely evaporated (*SI Appendix*, Fig. S10*D*). The drying process was recorded using a CCD camera mounted on a Nikon TE 2000-U inverted microscope in the brightfield mode.

In previous experiments on evaporation in microchannels and nanochannels (7, 11), it was observed that the menisci recede from the channel entrance until all the water was evaporated. In contrast, we found that the menisci remained pinned at the channel entrance while a small bubble appeared at one end of the channels and rapidly moved into the channel (Fig. 2). High-speed imaging revealed that the meniscus first receded a distance up to 4 or 5 μm into the nanochannel. Next, water reappeared at the entrance of the nanochannel, entrapping a bubble (see Fig. 2 $t = 0$ s and *SI Appendix*, Figs. S16 and S17). The bubble then rapidly moved into the channel. In a short timescale (*ca.* 50 ms), the bubble stabilized at a certain location inside the channel and grew gradually as evaporation continued. Furthermore, when one end of the bubble reached the center of the nanochannel, it exhibited a tendency to split into two bubbles, which then occupied symmetric locations in the nanochannel (Fig. 2). These two bubbles then continued expanding until all the water in the nanochannel disappeared due to evaporation.* Interestingly, this bubble splitting occurred only in nanochannels smaller than 70 nm in height. In larger nanochannels, the bubbles did not split, although a clear pinching of the bubble was visible at the center of the channel (*SI Appendix*, Fig. S15). These observations were repeatable in all the nanochannel devices regardless of surface plasma treatment, fresh or stored surfaces, and before/after KOH etch. The observed bubble entrapment, movement, and expansion were not sensitive to the gas content in water, the ambient temperature, or pressure. The same phenomena were observed using degassed water at various temperatures (25–70 °C) under atmospheric pressure. Similar behavior also occurred when the water-filled nanochannel device was placed in a vacuum chamber (200 mTorr) and the liquid was allowed to evaporate, where the surrounding gas was primarily water vapor instead of air. Presumably, the entrapped bubble primarily comprised water vapor (vapor pressure *ca.* 20,000 mTorr) in the low-pressure case. Furthermore, these observations were repeatable with other liquids, including ethanol, isopropanol, acetone, and hexane, both under atmospheric conditions and under vacuum.

*In 20-nm nanochannels, the outward ends of these two split bubbles reached nanochannel entrance at $t = 0.85$ s. Vapor bubbles disappeared after that time (see Fig. 4*A*).

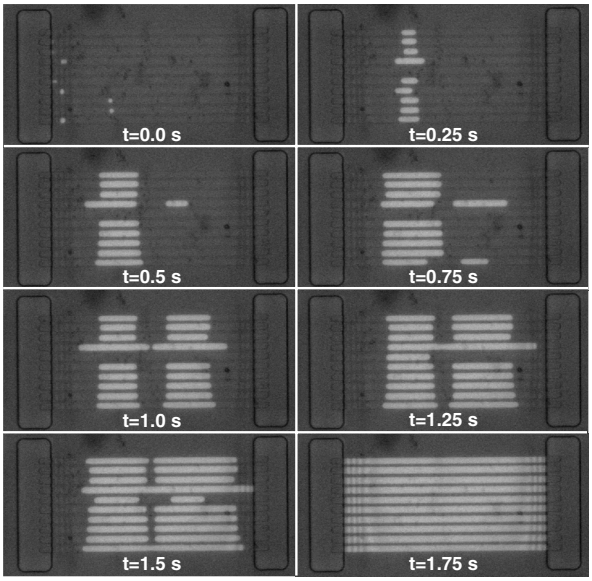

Fig. 2. Cavitations in 58-nm nanochannels. Instead of menisci recession, vapor bubbles occurred at the left entrance and two menisci were pinned at the entrances. Bubbles then moved toward the center of the channel and started expansion. There are two symmetric stationary positions in each channel that bubbles prefer to stay.

There are many questions that are raised by these observations: How does the bubble occur at the channel entrance and why does it grow inside the nanochannel? What determines the bubble growth rate? Why are there stable locations in the nanochannels where the bubbles are stationary, and why are these locations symmetric? What drives the bubbles to these stable locations and what governs the stability? Why do some of the bubbles split and others do not? We will now attempt to answer these questions by invoking an experimental and theoretical combined study.

First, we observed that the appearance of the initial small bubbles had a strong correlation with the presence of local expansions at the nanochannel entrances, which were produced by SF_6 plasma etching before releasing the sacrificial polysilicon layer (see *SI Appendix*). As shown in Fig. 3, the nanochannel height at the channel entrance was about 20-nm larger than that in the center and gradually decreased to the center value within a few microns. In the nanochannels with a tapered entrance, the bubble entrapment phenomenon was consistently observed. In contrast, bubbles were never observed in nanochannels without the local expansions (where the SF_6 etch step was omitted). Instead, menisci receded from one or both sides of such uniform-height channels, being consistent with the previous studies on negative pressure and evaporation in nanochannels (7, 11). These observations suggest that the expansion at the entrance of the nanochannels played a role in remerging of the menisci, resulting in the entrapped bubble that subsequently moved into the nanochannel and expanded.

In nanochannels with local expansions, expansion of the entrapped bubble may be facilitated by the small radius of the menisci at the nanochannel entrance that result in a huge negative pressure ($P_l = P_{\text{air}} - \frac{2\sigma}{h}$) inside the liquid (7, 12). Taking water as an example, the corresponding water pressure in 20- to 120-nm 1D confined nanochannels varies from −7 to −1 MPa. Water is metastable at such negative pressures, which may facilitate the growth of the entrapped bubbles that act as the nuclei. The role of the menisci at the nanochannel entrance in the cavitation process was confirmed by a control experiment where water was reintroduced into the microchannel before bubbles occupied the

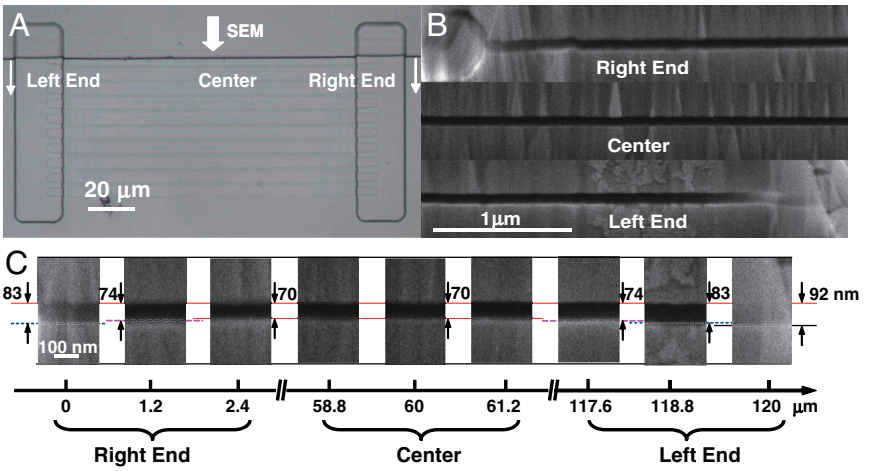

Fig. 3. Nanochannel cross-sectional images along the channel length direction. (*A*) Top view image of a set of nanochannels. The first nanochannel was "cut" by dry etching method for SEM cross-section (see *SI Appendix*). (*B*) SEM cross-sectional images of the nanochannel at the right end, center, and left end. (*C*) Height change along channel length direction. The maximum height difference is 22 nm.

entire nanochannel. Because the reintroduction of water in the microchannels removes the evaporation-induced menisci at the nanochannel entrance, water should no longer be under negative pressure and the bubbles should collapse. This scenario was indeed what we observed—i.e., all bubbles disappeared immediately after water introduction, suggesting that the final bubble content is water vapor and this bubble expansion process is an evaporation-induced cavitation. In contrast, when water was reintroduced after nanochannels were dry, air bubbles were trapped and disappeared slowly (after several minutes) due to the time required to dissolve air in the water. Thus, we can confirm that the bubbles in the nanochannels were comprised primarily of water vapor and stabilized by the negative pressure due to the menisci at the channel entrances, at least in the later stages of evaporation when the bubbles had moved to stable positions within the nanochannels.

We also compared the rates of evaporation of water in 20-nm nanochannels in the presence and absence of cavitation, as deduced from the change in the amount of liquid water in the channels as a function of time (Fig. 4*A*). In the nanochannels where the cavitation was absent, evaporation occurred faster than the theoretical prediction based on pure vapor diffusion in the nanochannel, which may be attributed to the presence of a water film along the corners of the rectangular cross-sections of these nanochannels (11). However, the total water evaporation length, L, still followed $L \propto \sqrt{t}$ behavior indicative of a diffusion-governed process. In contrast, in the channels where cavitation occurred, bubble length followed $L \propto t$ behavior. This linear relationship indicates a constant, faster transport mechanism, caused by presence of the meniscus at the nanochannel entrance. However, when one side of the vapor bubbles reached the end of the nanochannel, the bubble confined within the channel disappeared and the menisci receded from both directions, similar to the case without cavitation. In this regime (termed Evaporation after Cavitation in Fig. 4*A*), the evaporation rate was significantly lower than that in the former case: The initial evaporation rate in the presence of cavitation inside nanochannels was almost 35 times larger than the later evaporation rate without cavitation. This constant evaporation rate was also observed in other nanochannels with different heights (Fig. 4*B*). Although growth of confined bubbles in nanochannels has not yet been reported, the growth of confined vapor bubbles reported in larger microchannels typically does not exhibit a constant evaporation rate (13). Instead, the growth rate of confined vapor bubbles in microchannels is typically observed to increase with time, consistent with the momentum-governed bubble growth theory (13).

Because the two menisci are pinned at the nanochannel entrances, any volume increase of the vapor bubble indicates that the same volume of water is removed from the channel. However, to conserve mass, the volume of water entering the vapor phase must be larger than the volume of liquid by a factor equal to the density ratio, $\frac{\rho_l}{\rho_v}$, which is equal to 5×10^4. Because the bubble volume does not increase by such a factor, one concludes that most of the water must be removed at the nanochannel entrances where the menisci are pinned. Fig. 4*C* shows that the bubble growth rate is inversely proportional to the channel height, suggesting that the rate of evaporation at the menisci at the entrance govern the evaporation rate. The evaporation processes can be treated as a steady-state vapor diffusion problem that is governed by the Laplace equation (14). It can be further simplified by using the concept of a series of diffusion resistances. There are three resistances between the nanochannel entrance and the atmosphere: (*i*) diffusion resistance around the nanochannel entrance R_n; (*ii*) diffusion resistance along the microchannel R_m; and (*iii*) diffusion resistance from the reservoir to the atmosphere (see *SI Appendix* and Fig. S18). The consequent water evaporation rate inside the nanochannel can thus be expressed as

$$U = \frac{1}{2Nw_n h_n \rho_w} \frac{\rho_v(\phi_n - \phi_\infty)}{R_n + R_m + R_r}, \quad [1]$$

where N is the total number of nanochannels; w_n and h_n are the nanochannel width and height, respectively; ρ_v is the saturated water vapor density at 25 °C; ρ_w is the liquid water density;ϕ_n is the relative humidity at the nanochannel entrance; and ϕ_∞ is the relative humidity of ambient atmosphere. These three resistances do not include the diffusion resistance along the nanochannel because the meniscus is pinned at the entrance. It is this resistance that causes the slow square root of time dependence of normal evaporation process because the resistance continuously increases as the meniscus recedes away from the channel entrance. In our experiments, all three resistances are constant, leading to a constant evaporation rate for a given geometry and humidity condition. As can be seen, the resistance of the microchannel, R_m, dominates over the corresponding resistances of the nanochannel and the reservoir (see *SI Appendix*). The other two are at least one order of magnitude smaller than this resistance. Therefore, Eq. **1** is further simplified as

$$U = \frac{4Dw_m h_m \rho_v(\phi_n - \phi_\infty)}{Nl_m w_n h_n \rho_w}, \quad [2]$$

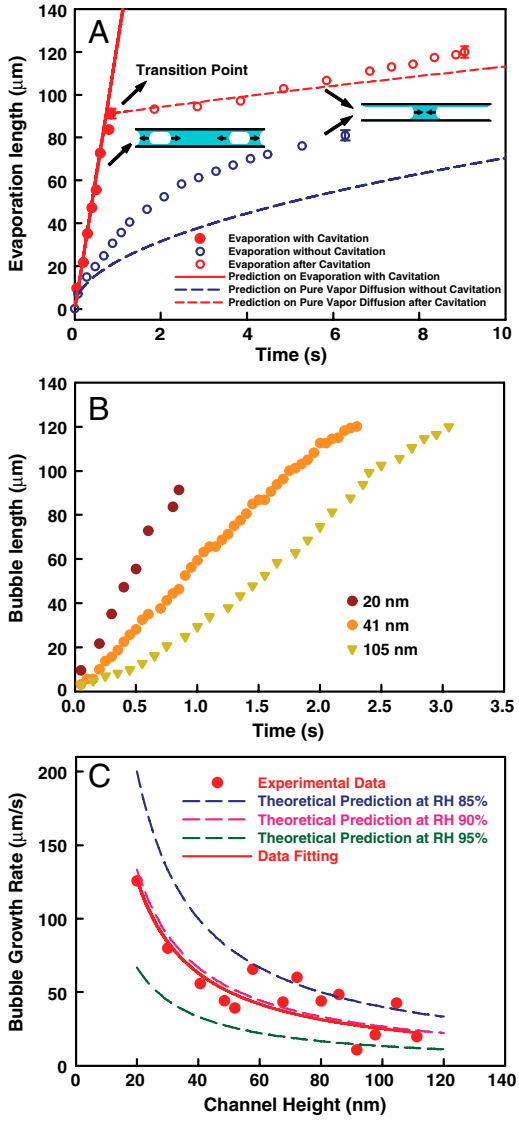

Fig. 4. Vapor bubble growth rate in the presence of cavitation. (*A*) Total vapor bubble length (water evaporation length) as a function of time in 20-nm nanochannel with/without cavitation. Unlike normal evaporation where $L \propto \sqrt{t}$, evaporation with cavitation follows $L \propto t$, leading to a significant increase in evaporation rate. (*B*) Total vapor bubble length (water evaporation length) as a function of time in 20-, 41-, and 105-nm-deep nanochannels. Vapor bubbles always expand linearly with time, which is significantly different from vapor bubble growth in confined microchannels (13). (*C*) Experimental results as well as theoretical predictions of bubble growth rate in nanochannels with heights from 20 to 120 nm. Bubble growth rate decreases as the nanochannel height increases. Each experimental point represents the average growth rate in five nanochannels. The standard deviation is within 4% of the mean value, which is similar to the symbol size and thus not shown in the plot. The solid line represents a fit with Eq. **2**, which gives the relative humidity 90.6%.

where D is the diffusion coefficient of water vapor in air; and w_m, h_m, and l_m are the microchannel width, height, and length, respectively. Eq. **2** indicates that bubble growth rate U is inversely proportional to the height of the nanochannel, $U \propto 1/h_n$. The agreement in the trends between the experimental data and our theoretical analysis (Fig. 4*C*) suggests that this process is indeed limited by evaporation at the nanochannel entrances.

It is also of interest to understand the bubble motion during the cavitation process from the entrance of the channel toward the center. The bubbles preferred to move to two symmetric locations on either side of the center line, which are highly dependent on the channel height (Fig. 5*A*). For larger channel heights, the preferred location moved closer to the center of the channel. It may be anticipated that the stationary position of the bubble can be explained by competing transport phenomena. Because the continuous evaporation at two ends of the channel requires heat transfer from surroundings, we examined whether the balance of thermocapillary motion of the bubble under a temperature gradient and the convective motion due to evaporation could predict the stationary bubble location. A one-dimensional steady-state heat transfer model can be used to estimate the temperature distribution along the channel length direction (see *SI Appendix*). The temperature gradient

$$\frac{dT}{dx} = \frac{(l_n - 2x)}{l_n} \frac{U\rho_w h_n h_{\text{latent}}}{k_o d_o}$$

reaches its maximum value (1,000 K/m) at the channel entrance and linearly decreases to zero at the center of the channel.

Such a temperature difference around the bubble results in a nonuniform surface tension, leading to a net water flow (referred as thermocapillary flow) that drives water around the bubble toward the cold side. For the circular-disk-shaped bubble, the corresponding thermocapillary flux is

$$J_{\text{thermocapillary}} = C \frac{r}{\mu} \frac{d\sigma}{dT} \frac{dT}{dx} w_n h_n,$$

where C is a geometry-related constant, μ is the viscosity of water, r is the radius of the bubble, and T is the temperature (see *SI Appendix*).

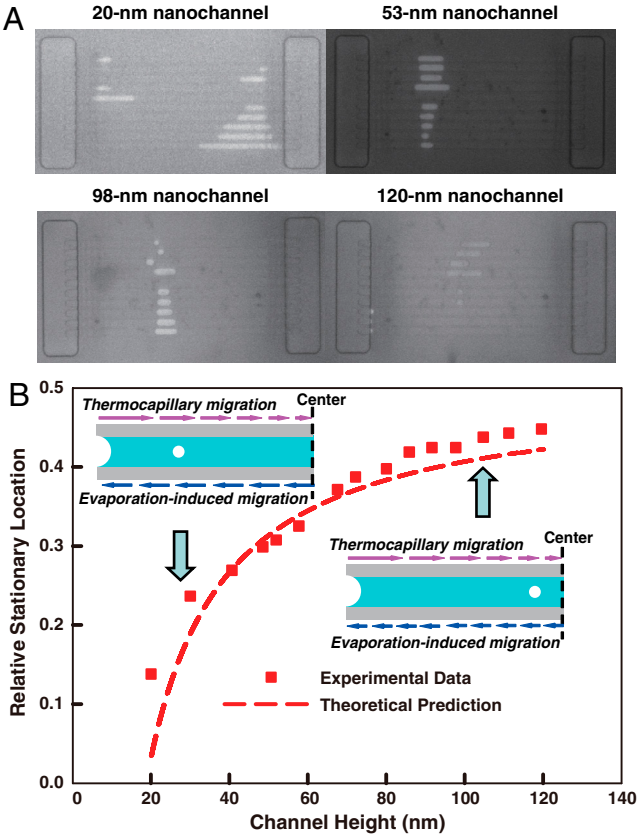

Fig. 5. Bubble stationary locations in 120-μm-long nanochannels. (*A*) Snapshots of stationary locations in 20-, 52-, 98-, and 120-nm-deep nanochannels. (*B*) Experimental results as well as theoretical prediction of bubble stationary locations in nanochannels with heights from 20 to 120 nm. As the channel height increases, bubbles prefer to stop closer to the middle of the nanochannel. These stationary locations are determined by two competing migrations—i.e., the thermocapillary migration and the evaporation-induced migration.

Ideally, such water flow will push the bubble toward the hot side—i.e., the center of the channel in our case. However, water continuously evaporates at the channel entrance with a flux $J_{\text{evaporation}} = Uw_n h_n$. If the thermocapillary-driven mass flux exactly compensates the evaporation-induced mass flux at a certain location, a bubble will become stationary. The location of this stationary point can be estimated to be

$$X = \frac{1}{2}\left(1 - \frac{\mu k_o d_o}{Cr\rho_w h_{\text{latent}} h_n \frac{d\sigma}{dT}}\right), \quad [3]$$

where k_o is the thermal conductivity of silica, d_o is the thickness of the capping silica layer, and h_{latent} is the latent heat of water evaporation. $X = x/l_n$ is the relative stationary position with $X = 0.5$ the midpoint of the nanochannel.

Eq. **3** indicates that the bubble stationary position is determined by the device geometry and material properties and is thus independent of the relative humidity as well as the evaporation rate. This theoretical analysis is consistent with our observation because the bubble stationary location in a 74-nm channel did not change when repeating the experiment with evaporation rates ranging from 60 to 21 μm/s due to changes in humidity. This stationary location also did not change when the experiment was performed under vacuum. This independence results from the intrinsic relationship between the evaporation rate and the temperature gradient; i.e., evaporation at the nanochannel entrance determines the temperature gradient along the nanochannel and enhancing the evaporation rate simultaneously enhances the thermocapillary flow. There are also other possible mechanisms to explain these bubble stationary locations, such as the competition between evaporation-driven flow and geometry-induced (or surface roughness/surface composition induced) pressure-driven flow. However, the channel topography study showed that the required geometry (continuous constriction from the entrance to the center) does not exist (see *SI Appendix*). Furthermore, predictions based on those mechanisms cannot explain the independence of the bubble position on the evaporation rate (see *SI Appendix*). Assuming a confined bubble with a diameter of 2 μm, the theoretical prediction based on the thermocapillary flow (Eq. **3**) shows excellent agreement with the experimental results (Fig. 5*B*). Therefore, it appears that the stationary bubble location results from a balance between a constant evaporation-induced liquid flow toward the nanochannel entrance and an opposing thermocapillary-driven flow toward the nanochannel center. What is remarkable is the precision and control of nanoscale bubble motion through such a competition.

The above analysis for bubble dynamics can also qualitatively explain bubble splitting in larger nanochannels. Because σ monotonically decreases from the entrance to the center (see the temperature analysis above), $P_{\text{liquid}} \approx P_{\text{vapor}} - \frac{2\sigma}{h_n}$, reaches its maximum at the center of the channel. The liquid pressure difference ΔP_{liquid} between the center of the channel and the surroundings will press the bubble locally, resulting in a deformation in the bubble at the center of the nanochannel. This deformation could serve as a perturbation to induce Plateau–Rayleigh instability. Because ΔP_{liquid} is inversely proportional to h_n, the deformation/perturbation increases with the decreasing channel height. Consequently, bubbles in smaller channels prefer to split, whereas bubbles in bigger channels do not.

Although the above model explains many of the observations, the mechanism of bubble emergence at the channel entrance and stability of bubbles inside the nanochannels are still unclear. The remerging of water menisci at the entrance results in trapped bubbles comprising air, vapor, or air–vapor mixture. These entrapped bubbles serve as stable nuclei for cavitation in these 1D confined nanochannels. However, for nanochannels with uniform properties and local expansions at both entrances, these trapped gas bubbles should not grow because they are confined by the channel to a size smaller than the critical bubble nucleation size required for bubble growth (the channel height at the nanochannel entrance is larger than that at the bubble location). Anomalous bubble stability has also been observed in another case; several studies have reported stable spherical-cap-shaped air nanobubbles on hydrophobic surfaces. Surface tension change due to contamination (15, 16) and/or adsorption of hydroxide ions (17) at the air/water interface, as well as continuous influx of gas due to the gas attraction toward the hydrophobic surface (18), have been proposed to explain the stability of these nanobubbles larger than approximately 5 nm. Because our nanochannel surface is always hydrophilic, cavitation also occurred during water evaporation under vacuum, and the bubbles immediately collapsed upon reintroduction of water into the device, continuous influx of gas is unlikely the reason for bubble stability in nanochannels. However, it is possible that the meniscus at the channel entrance differs from that at the bubble/liquid interface, in terms of surface tension due to contamination and/or ion adsorption, or meniscus curvature due to disjoining pressure (19) and other factors. Such differences may result in a larger pressure drop at the nanochannel entrance than that at the bubble/liquid interface, resulting in stable bubbles inside the nanochannel. (Surface tension also changes due to temperature difference along the nanochannel, but such change is not big enough to yield a lower liquid pressure at the entrance.)

The other aspect that remains elusive is the reason for bubble entrapment that leads to cavitation. Although there is a strong correlation between cavitation and presence of the local expansion at the channel entrance, we do not know how the local expansion causes water to reappear at the channel entrance. Instability around the deformed meniscus observed on the horizontal plane due to channel height change is certainly a possible reason (see *SI Appendix*, Figs. S16 and S17). Remerging of liquid thin film from top and bottom surfaces due to thin-film flow at the local expansion could be another potential reason. Because the nanochannel surface is hydrophilic, we expect a film of water on the nanochannel entrance ahead of the meniscus. Water flow in this thin film toward the entrance has been considered as a major reason for accelerated evaporation in microporous media (12). This thin-film liquid flow may result in the formation of two capillary ridges at the local expansion because of evaporation-induced temperature difference and the channel topography (20), causing remerging of water and trapping surrounding gas. This temperature difference and the local expansion may also facilitate capillary condensation (21, 22) close to the entrance and thus trap a bubble. These are a few possible hypotheses, and there could be others as well. At this point, we do not understand the mechanism of bubble emergence, but our observations confirm that cavitation can indeed occur in nanoscale confined liquids, which may have bearing on several phenomena.

It is known that cavitation can occur in plant xylem, which is an array of parallel microchannels (stem part) in series with many nanopores at their entrances (leaf part) that are used for water transport. These microchannels are connected with each other through intervessel nanochannels (see *SI Appendix*, Fig. S22). Cavitation in xylem is currently thought to occur when the liquid meniscus at the entrance of these intervessel nanochannels recedes to the xylem (3, 4, 23) (*SI Appendix*, Fig. S22*A*). Our observations suggest the possibility of air bubbles being nucleated at the nanochannel entrance and transported into the xylem while the meniscus remains pinned at the entrance of the nanochannels (*SI Appendix*, Fig. S22*B*), which could be another possible mechanism for heterogeneous liquid cavitation under negative pressure (3, 24). Our analysis also suggests that, no matter where the original bubble occurs, the cavitation bubble growth rate in plant xylem likely depends on the water evaporation rate on the surface. Direct visual observations of cavitation in nanoscale channels could help gain deeper insight into cavitation in these

systems, which is currently studied using indirect acoustic methods (25) or hydraulic conductance measurements (26), or in hydrogel systems (24).

The presence of cavitation during evaporation in nanochannels and the consequent high evaporation rate also suggests that it could be a possible mechanism for fast drying of porous materials, which is an important engineering process in various applications such as paper, textile, food, and medicine (27). The structure of pores in such materials is a network of micro- and nanochannels. It has been proposed that counterflow of water from the thick corner film in these channels is responsible for the fast evaporation (28). Our observations suggest an alternative mechanism whereby evaporation-induced cavitation inside the nanochannel increases the evaporation rate because the evaporating meniscus is pinned at the channel entrance and the entire channel is used to transport water to the entrance (see *SI Appendix*, Fig. S23).

In conclusion, cavitation due to evaporation-induced negative pressure has been directly observed in transparent nanofluidic channels. We found that local expansions at the nanochannel entrances could result in entrapped bubbles that act as nuclei for such cavitation. The growth rate of vapor bubbles during this confined cavitation process only depends on the water evaporation at the nanochannel entrance. The resulting water evaporation is not diffusion limited and can thus occur at a much faster rate than evaporation without cavitation. There are certain stationary positions for vapor bubbles inside the nanochannel, which are determined by two competing fluidic flows: evaporation-induced hydraulic flow and thermocapillary-driven flow. Our visual study combined with theoretical analysis could form the foundation for further investigation of cavitation in plants and fast drying of micro/nanoporous materials.

ACKNOWLEDGMENTS. We thank S. Morris and V. Carey for their valuable discussions on cavitation formation and bubble dynamics. This work was supported by Basic Energy Sciences, Department of Energy (DE-AC02-05-CH11231), National Science Foundation (NSF) Center for Scalable and Integrated Nanomanufacturing (DMI-0327077), and NSF Center of Integrated Nanomechanical Systems at University of California, Berkeley (NSF EEC-0425914). Devices were fabricated at the Microfabrication Laboratory at the University of California, Berkeley.

1. Dixon HH (1914) *Transpiration and the Ascent of Sap in Plants* (Macmillan, London).
2. Trevena DH (1987) *Cavitation and Tension in Liquids*, ed A Hilger (Bristol, Philadelphia).
3. Tyree MT (1997) The Cohesion-Tension theory of sap ascent: Current controversies. *J Exp Bot* 48:1753–1765.
4. Tyree MT (2003) Plant hydraulics: The ascent of water. *Nature* 423:923–923.
5. Ursprung A (1915) About the cohesion of water in Farnanulus (Translated from German). *Ber Dtsch Bot Ges* 33:153–162.
6. Renner O (1915) Theoretical and experimental theory of water movement to Kohasions (Translated from German). *Jahrbuchfur wissenschaftliche Botanik* 56:617–667.
7. Tas NR, Mela P, Kramer T, Berenschot JW, van den Berg A (2003) Capillarity induced negative pressure of water plugs in nanochannels. *Nano Lett* 3:1537–1540.
8. Zhang RJ, Ikoma Y, Motooka T (2010) Negative capillary-pressure-induced cavitation probability in nanochannels. *Nanotechnology* 21:105706.
9. Karnik R, Castelino K, Fan R, Yang P, Majumdar A (2005) Effects of biological reactions and modifications on conductance of nanofluidic channels. *Nano Lett* 5:1638–1642.
10. Karnik R, Castelino K, Duan CH, Majumdar A (2006) Diffusion-limited patterning of molecules in nanofluidic channels. *Nano Lett* 6:1735–1740.
11. Eijkel JCT, et al. (2005) Strongly accelerated and humidity-independent drying of nanochannels induced by sharp corners. *Phys Rev Lett* 95:256107.
12. Wheeler TD, Stroock AD (2008) The transpiration of water at negative pressures in a synthetic tree. *Nature* 455:208–212.
13. Kenning DBR, Wen DS, Das KS, Wilson SK (2006) Confined growth of a vapour bubble in a capillary tube at initially uniform superheat: Experiments and modelling. *Int J Heat Mass Transf* 49:4653–4671.
14. Deegan RD, et al. (1997) Capillary flow as the cause of ring stains from dried liquid drops. *Nature* 389:827–829.
15. Johnson BD, Cooke RC (1981) Generation of stabilized microbubbles in seawater. *Science* 213:209–211.
16. Dressaire E, Bee R, Bell DC, Lips A, Stone HA (2008) Interfacial polygonal nanopatterning of stable microbubbles. *Science* 320:1198–1201.
17. Jin F, Li JF, Ye XD, Wu C (2007) Effects of pH and ionic strength on the stability of nanobubbles in aqueous solutions of alpha-cyclodextrin. *J Phys Chem B* 111:11745–11749.
18. Brenner MP, Lohse D (2008) Dynamic equilibrium mechanism for surface nanobubble stabilization. *Phys Rev Lett* 101:214505.
19. Sweeney JB, Davis T, Scriven LE, Zasadzinski JA (1993) Equilibrium thin-films on rough surfaces.1. Capillary and disjoining effects. *Langmuir* 9:1551–1555.
20. Kalliadasis S, Bielarz C, Homsy GM (2000) Steady free-surface thin film flows over topography. *Phys Fluids* 12:1889–1898.
21. Iwamatsu M, Horii K (1996) Capillary condensation and adhesion of two wetter surfaces. *J Colloid Interface Sci* 182:400–406.
22. Tuller M, Or D, Dudley LM (1999) Adsorption and capillary condensation in porous media: Liquid retention and interfacial configurations in angular pores. *Water Resour Res* 35:1949–1964.
23. Zimmermann MH (1983) *Xylem Structure and the Ascent of Sap* (Springer, Berlin), pp 96–104.
24. Wheeler TD, Stroock AD (2009) Stability limit of liquid water in metastable equilibrium with subsaturated vapors. *Langmuir* 25:7609–7622.
25. Milburn JA, Johnson RPC (1966) Conduction of sap. 2. Detection of vibrations produced by sap cavitation in Ricinus xylem. *Planta* 69:43–52.
26. Tyree MT, Sperry JS (1989) Vulnerability of xylem to cavitation and embolism. *Annu Rev Plant Physiol Plant Mol Biol* 40:19–38.
27. Whitaker S (1998) Coupled transport in multiphase systems: A theory of drying. *Adv Heat Transf* 31:1–103.
28. Yiotis AG, Boudouvis AG, Stubos AK, Tsimpanogiannis IN, Yortsos YC (2004) Effect of liquid films on the drying of porous media. *AIChe J* 50:2721–2737.